PERSPECTIVE

CrossMark

Carbon Permeation: The Prerequisite Elementary Step in Iron-Catalyzed Fischer–Tropsch Synthesis

Rui Gao[1,2,3] · Xingchen Liu[1,2,6] · Zhi Cao[1,2,4] · Xing-Wu Liu[1,2] · Kuan Lu[1,2] · Ding Ma[5] · Yong Yang[1,2] · Yong-Wang Li[1,2] · Roald Hoffmann[6] · Xiao-Dong Wen[1,2]

Abstract

Carbon permeation into iron, a very important initial stage in iron-catalyzed heterogeneous reactions such as Fischer–Tropsch synthesis (FTS), is explored theoretically, to extend our thermodynamic and kinetic understanding of the process. The interaction of C atoms with five model surfaces (Fe (100), (110), (111), (211), (310)) was studied in six distinct ways. In the first, the random deposition of C atoms on the Fe surfaces was simulated by molecular dynamics, with C atoms released gradually. It shows that the early stages of carburization is a C permeation process, without much disturbance to the Fe surfaces. In the second approach, C atoms were approached to the surfaces sequentially. They bind readily (by 7–9 eV per C) to the surfaces, but to a different extent—strongest on Fe (100), and weakest on Fe (111). Addition of further C atoms proceeds with a slightly decreasing magnitude of the chemisorption energy, because of the increasing positive charges on the Fe atoms. At a certain coverage, different on each surface, C atoms prefer in calculation to go subsurface. C_2 units formed on some of the surfaces. In a third approach, detailed transition paths of C permeation subsurface were calculated, with associated barriers in the order Fe (100) > (111) > (310) > (211) > (110). Differences in stacking geometries of the Fe layers in these surfaces appear to be the main cause of the variation. Comparing C permeation with surface migration on clean surfaces, the barrier of the former is smaller than that of the latter for most of the surfaces, except Fe (111). At intermediate C coverage, the (100) surface also prefers migration to permeation. In a fourth approach, we calculate that with increasing carbon chemical potential, the surface energies of iron (110), (111), and (211) surfaces decrease, while those of (100) and (310) first decrease, then increase. Based on these surface energies, a Wulff construction of nanoparticle facets is made. In a fifth approach, the position in energy of the d-band centers of the Fe surfaces upon C permeation was studied. For all the surfaces, the d-band centers move away from the Fermi level with increasing C coverage, and start to resemble those of the bulk carbide phases at high C coverage. In the last approach, we show that C permeation not only lowers the barriers of model reactions for CH_4 formation and C–C chain propagation, two competing processes in FTS, but also changes the selectivity

---

Rui Gao, Xingchen Liu, and Zhi Cao have contributed equally to this work.

✉ Roald Hoffmann
rh34@cornell.edu

✉ Xiao-Dong Wen
wxd@sxicc.ac.cn

1   State Key Laboratory of Coal Conversion, Institute of Coal Chemistry, Chinese Academy of Sciences, Taiyuan 030001, China

2   National Energy Center for Coal to Liquids, Synfuels CHINA Co., Ltd, Huairou District, Beijing 101400, China

3   College of Chemistry and Chemical Engineering, Inner Mongolia University, Hohhot 010021, China

4   Department of Chemistry, University of California, Berkeley, CA 94720, USA

5   College of Chemistry and Molecular Engineering, Center for Computational Science and Engineering, Peking University, Beijing 100871, China

6   Department of Chemistry and Chemical Biology, Cornell University, Baker Laboratory, Ithaca, NY 14853-1301, USA

of the two competing processes. At high C coverage, chain propagation becomes preferred. A general picture emerges of C permeation on Fe surfaces as a stepwise process with opposite thermodynamic and kinetic preferences.

Graphical Abstract
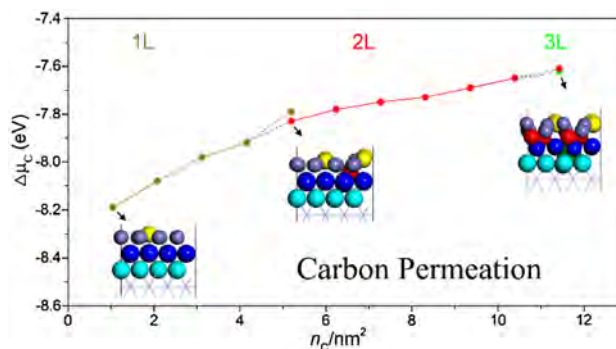
Keywords Iron catalyst · Fischer–Tropsch synthesis · DFT · Carbon permeation

1 Introduction

Global environmental changes and energy demands have led to broad interest in the selective conversion of syngas (CO/H_2) into liquid fuels and value-added chemicals [1]. The Fischer–Tropsch synthesis (FTS, $CO + 2H_2 \rightarrow C_xH_y + H_2O$) offers a promising pathway to meet this challenge, and much effort has been devoted to optimizing the energetic efficiency and selectivity of this reaction in the production of linear paraffins, α-olefins, and other oxygenated compounds [2–5]. Among existing FTS catalysts, iron-based ones are particularly attractive in industrial applications, due to their high activity and low cost [6–8]. The activity of iron-based catalysts has been attributed to complex mixtures of iron carbides (Fe_xC_y) [9, 10], formed from reducing and carburizing the Fe_2O_3 precursor [11, 12]. The morphology, phase composition, and electronic properties of the resulting Fe_xC_y mixture are proposed to directly influence catalytic activity [13–17]. Yet we need to know more the details of carbon permeation into iron, the early stage of carburization. In this report, we provide an initial study of the microscopic thermodynamic and kinetic nature of carbon permeation, and how carbon permeation (or penetration; we use the words interchangeably in this paper, and define them in further detail below) dictates the morphology, phase composition, and electronic properties of iron catalysts.

The initial step in use of a catalyst is carbon adsorption on Fe surfaces in some cases; this process has been studied both experimentally [18–20] and theoretically [21–28]. Most investigations focus on aspects of low-index (≤1) surfaces of Fe (100), (110) and (111), such as adsorption sites, carbon coverage and diffusion. These studies provide an understanding of the initial step of carbon permeation in microscopic

size regimes. Yet contributions that correlate these properties with the catalyst morphology, electronic properties, and catalytic activity/selectivity, remain sparse. Some studies on metallurgy (macroscale) have reported bulk phase transformations induced by carbon permeation [29]. However, many of the experiments carried out are performed at high temperature (over 600 °C), in near-vacuum conditions, and over a long time-scale; these do not represent typical thermocatalytic conditions of the FTS reactions. Hence, investigation of carbon permeation under FTS reaction conditions at both microscale and macroscale should provide insights into the catalytic process, aiding in the design of novel iron-based catalysts with improved catalytic performances.

In FTS, although CO is a major source of surface C for Fe carburization through the Boudouard Reaction [8, 30], Fe carburization can also occur through other carbon sources, such as CH_4 [31] and other saturated hydrocarbons [32]. In the steel industry, there has been a long history of using "carbon potential" to determine the carburizing potential of the atmosphere on iron, a mode of analysis which takes into account the composition of various gas constituents (CO, CH_4, CO_2, etc.) [33].

FTS is well-known for the complexity of the surface species, which include hydrogen, CO, water, and most importantly, hydrocarbons with a wide carbon number distribution. Therefore, there could be many C sources during FTS reaction; all of them may contribute to the Fe carburization. Using ab initio atomistic thermodynamics to study the iron carbide phases in FTS, de Smit et al. [17] found that the stable carbide phases also are sensitive to the carbon chemical potential (μ_C, or carbon potential for short) imposed by the FTS environment. Since in the carburization of Fe, the C element has to go into the

interstices of bulk Fe in atomic form, following the lines of these studies, in this work we do not choose any particular carbon source, but think of carburization as the permeation of C atoms into the Fe lattices, with the C composition measured by carbon potential (μ_C).

Another factor to consider in Fe carburization in FTS is naturally oxygen, which can be generated from CO dissociation. In order to study carburization of Fe nanoparticle in the presence of syngas, our group used environmental TEM to directly record the carburization process of a metallic iron particle of 20 nm in diameter under a CO and H_2 atmosphere with molar ratio of H_2 to CO equal to 4 [34]. During the initial one hour exposure, iron carbide clusters formed on the surfaces of the iron nanoparticle, but no oxides could be detected. This indicates that oxygen atoms are quickly removed in the form of water during the carburization process and their surface coverage is too low to oxidize iron. During the entire course of the in-situ experiment (6 h), the majority of nanoparticles were iron and iron carbides formed through in-situ carburization. This study suggests that after CO dissociation, oxygen atoms quickly reacted with H (also present on the surface) and desorb as water, and have little influence on the carburization process. Also, our recent study [35] shows that even without H_2, CO could remove surface oxygen on Fe surfaces by forming CO_2 at 150 °C. Therefore, the role of oxygen in C permeation is most likely only an indirect one: oxygen affects the C permeation by affecting the surface coverage of C atoms on the surface.

In this work, following our previous studies [36, 37], five important surfaces of bcc Fe (100), (110), (111), (310) and (211), are chosen to study carbon permeation of iron-based FTS catalysts via computational methods. Specifically, we try to understand the initial stages of the carbon adsorption and permeation process in several different ways from both a thermodynamic and kinetic perspective, and delineate the influence of carbon permeation on catalyst morphology, electronic structure evolution, and catalytic activity.

It is important for the readers to be aware of the limitation of this study. The C permeation into iron in FTS is a complicated process. In five out of six approaches to the C permeation problem, we use idealized (T → 0 K) conditions to model the early stage of C permeation with DFT, and move on to estimate activation energies and rate constants for motion between local thermodynamic minima. We then use these models to discuss how C permeation may affect catalyst morphology, electronic properties, and catalytic activity. Our simple models, while as realistic as we can make them, are based on local minima at idealized condition, and have much room for improvement. In a subsequent paper, we will look at more realistic models of carbon permeation at higher T, try to locate the global minima of C-permeated structures, and study the formation of possible new surface carbide phases.

2 Molecular Dynamic (MD) Simulation Methods

In this work, the "large-scale atomic/molecular massively parallel simulator" package [38] was used to perform a series of simulations with an MEAM potential [39]. MD simulations of the carbon permeation process were carried out in a three dimensional cell (Fig. 1), which is periodic only along x and y directions, with a free boundary in the z direction. The deposition of the carbon atoms was simulated with an NVE ensemble.

In the five models of Fe (100), (110), (111), (310) and (211) surfaces, the two bottom layers of the substrate were fixed, while other layers are allowed to move, with the temperature controlled using a Berendsen thermostat [40]. To be consistent, the five surface models used in the MD simulations have similar surface area (18–19 nm²/supercell), thickness (1.5–1.6 nm) and number of Fe atoms (about 2500).

In one of the six approaches to the problem, to mimic deposition, the C atoms were released to the surface one after another. Each carbon was initially placed in the vacuum region at a random position about 5 to 7 Å above the surface. At this initial height, the interaction between the introduced carbons and the underlying surface is negligible. The velocities of the deposited atoms were sampled from a Maxwell–Gaussian distribution with the most probable energy of 0.0259 eV at 300 K and 0.0494 eV at 600 K, as well as randomly selected incident angles. The time-step was set to 1 fs, and only one carbon atom was released toward the surface every 10,000 time-steps (10 ps). This period is sufficient for the previous carbon atom to fully diffuse into the iron substrate, should it prefer to do so [41, 42]. The C release procedure as described here is only applied in the first approach (MD simulation), but not in the other five approaches, which are based on DFT static calculations.
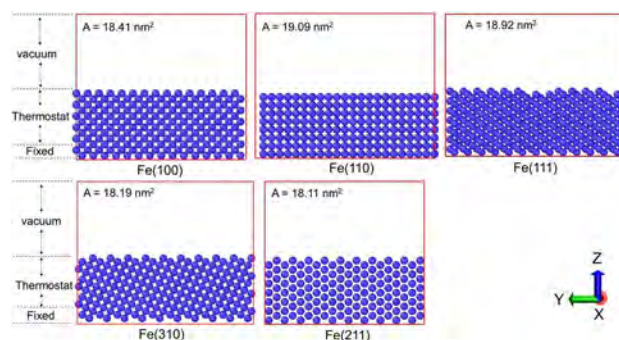

Fig. 1 Side view of the Fe (100), (110), (111), (310) and (211) surface models before the MD simulations. The boundary of the simulation cells is shown with red lines

3 DFT Methods

All DFT calculations were performed using the Vienna Ab Initio Simulation Package (VASP) [43, 44]. The electron–ion interaction was described with the projector augmented wave method [45, 46]. Electron exchange and correlation energies were treated within the generalized gradient approximation in the Perdew–Burke–Ernzerhof formalism (GGA-PBE) [47]. The plane wave basis cutoff was set to 400 eV, and the Monkhorst–Pack [48] k-point sampling was utilized. Electron smearing was employed according to the Methfessel-Paxton [49] technique, with a smearing width σ = 0.2 eV. Due to the large influence of magnetic properties on the adsorption energies, spin polarization was taken into consideration. To locate transition states (TS), we used the nudged elastic band (NEB) method [50]; a stretching frequency analysis was performed to verify whether a transition state is associated with a single imaginary frequency.

4 Energy and Rate Constants

The average carbon chemical potential for carbon adsorption (Fe + nC → nC/Fe) was calculated according to the equation $\Delta\mu_C = [E_{nC/slab} - E_{slab}]/n - E_C$, where $E_{nC/slab}$ is the total energy of the slab with n adsorbed carbon atoms in its equilibrium geometry, E_{slab} is the total energy of the bare slab, and E_C is the total energy of free atomic carbon in the gas phase. The barrier (E_a) and reaction energy (ΔE_r) were calculated by $E_a = E_{TS} - E_{IS}$ and $\Delta E_r = E_{FS} - E_{IS}$, where E_{IS}, E_{FS} and E_{TS} are the energies of the corresponding initial state (IS), final state (FS) and transition state (TS), respectively.

The surface energy of the carburized Fe surfaces is essentially the formation energy (E_f, J/m^2) of the carbon-permeated Fe surfaces (Fe + nC → nC/Fe). It is calculated as $E_f = [E_{nC/slab} - NE_{Fe/bulk} - n\mu_{C/gas}]/A$, where $E_{Fe/bulk}$ is the average energy of an Fe atom in the crystal, N is the number of Fe atoms in the Fe slab, and $\mu_{C/gas}$ is the energy of a carbon atom in the gas phase in FTS conditions, which is related to the gas composition and partial pressures [17]. For the definition of $\mu_{C/gas}$ in an atomic thermodynamic framework, please refer to our previous work [51, 52]. For the clean Fe surfaces (n = 0), E^0_f is made up of two parts, the top surface energy γ^0_t and the bottom one, γ^0_b. Under the same computational conditions (VASP-GGA-PBE) as in our previous work [36], γ^0_t represents the actual surface energy of the five surface models ($\gamma^0_t = \gamma^0$). Likewise, when n ≠ 0, the formation energy of the carburized surfaces also includes both the top and bottom surface

energies ($E_f = \gamma' + \gamma^0_b$). As the Fe atoms making up the bottom surfaces were fixed in these models in their bulk positions, we assume that the energy it takes to cut out such fixed bottom surfaces from Fe bulk (γ^0_b) is a constant, and does not depend on the number of C atoms added to the top surface. We then use the clean Fe surfaces (n = 0) to calculate this quantity as $\gamma^0_b = E^0_f - \gamma^0$. As such, the surface energy γ' can be computed by the equation $\gamma' = E_f - \gamma^0_b = E_f - (E^0_f - \gamma^0) = \gamma^0 + (E_f - E^0_f)$.

To distinguish rates of carbon permeation on different Fe surfaces, we computed the relevant rate constants (k) on the basis of transition state theory [53, 54]. The rate was calculated according to Eq. (1), in which k_B is the Boltzmann constant, T the reaction temperature, h Planck's constant, E_a the activation energy, and $q_{TS,vib}$ and $q_{IS,vib}$ the harmonic vibrational partition functions for the transition state and initial state, respectively. q_{vib} was obtained by Eq. (2), where ν_i is the frequency of each vibrational mode of the adsorbed intermediate derived from DFT calculations:

$$k = \frac{k_B T}{h} \frac{q_{TS,vib}}{q_{TS,vib}} e^{-E_a / k_B T} \tag{1}$$

$$q_{vib} = \prod_i \frac{1}{1 - e^{(-h\upsilon/k_B T)}} \tag{2}$$

5 Model Surfaces

The calculated lattice constant of the cubic Fe cell (bcc) is 2.831 Å, and the Fe–Fe separation is 2.452 Å. Unit cells p(4×4) for Fe (100) and (110), p(3×3) for Fe (111), as well as P(4×2) for Fe (310) and (211) were chosen in our DFT calculations, as shown in the top view of five surface models in Fig. 2. 3×3×1 k-point sampling was done for all
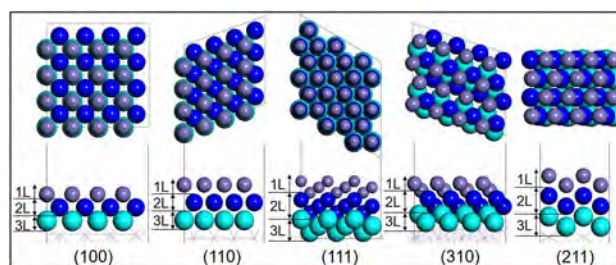

Fig. 2 Top and side view of the equilibrium structures of the Fe (100), (110), (111), (310) and (211) model surfaces from the DFT calculations. The 1st, 2nd and 3rd Fe atom layers are given in grayish blue, dark blue and cyan, respectively. In this figure and the figures following, we use purely for graphic reasons spheres of slightly different sizes to represent the Fe atoms in different layers (1st < 2nd < 3rd). The position of the C atoms adsorbed/permeated (1L/2L/3L) on/in the slab are defined on the left side of the structures, respectively

five surfaces. Among them, each of the Fe (100) and (110) models has 96 Fe atoms, of which 32 were fixed; Fe (111) has 90 Fe atoms, 27 fixed; the Fe (310) model has 88 Fe atoms, 24 fixed; and the Fe (211) surface model has 80 Fe atoms, 16 fixed. The top three layers of Fe atoms in these models are fully allowed to relax to account for potential surface reconstruction caused by carbon permeation.

Sites for C chemisorption and permeation may be classified by C–Fe separation, the coordination number of the site, and the relative geometric position of the adsorbed C with respect to the already occupied sites. The site that has the strongest binding energy for a given C atom is used in describing the energetics of adsorption and permeation. Although we could not scan over all the possible sites as each C atom is introduced (because of computational limitations), our testing of a variety of C binding sites ensures that the C atoms goes to a relatively favorable position.

Because of the complexity caused by the thickness and geometrical variety of the surface slabs, we need a clear definition of the positions of both Fe and C atoms. For this purpose, layers were defined; in Fig. 2, three layers of Fe atoms are shown for each of the five surface slabs. The Fe atoms in different layers are represented by different colors and sizes, and denoted as 1st, 2nd, and 3rd layer atoms, here and in the rest of the article. Because some of the surfaces are quite "open", there may be more than one sublayer of Fe atoms within a defined layer. An Fe layer in the (100) and (110) surface slab contains one sublayer, (111) three sublayers, and (310) and (211) two sublayers. The positions of the C atoms adsorbed/permeating are defined according to the Fe layers they enter, as 1L, 2L, and 3L. Each C layer corresponds to the entry/presence of one or more C atoms in the respective Fe layer (which may consist, as we noted, of several sublayers). Cutoff planes between 1L and 2L of the C atoms are defined as lying between the lowest sublayer of the 1st Fe layer and the highest sublayer of 2nd Fe layer. Cutoff planes between 2L and 3L are defined in a similar way.

6 Carbon Permeation from MD Simulations

To get an overall picture of the C permeation process at the Fischer–Tropsch (F–T) working temperature, the physical movements of the atoms were first simulated by MD at 300 and 600 K. We use the case of 600 K to discuss C permeation at high temperature F–T reaction conditions.

The C permeation process at FTS temperature can be roughly divided into two stages. At low C coverage (within the initial 300 ps MD simulation), the Fe reconstruction upon carbon permeation (Fig. 3a) is minimal for all the five Fe surfaces. At this stage, the Fe surfaces were not much perturbed. This shows that significant reconstruction did not happen in the initial stage of C permeation. However, at high
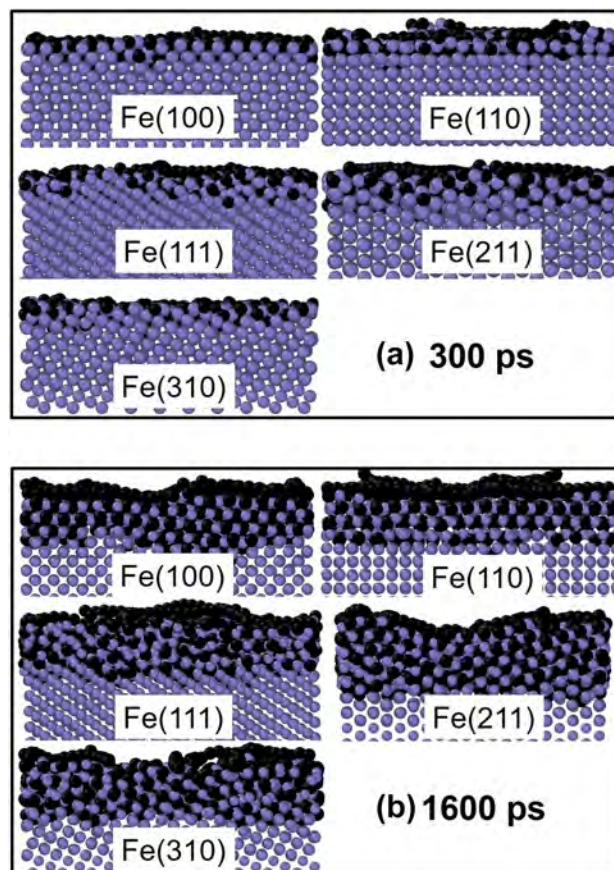

Fig. 3 Side-view structures of the five Fe surfaces after C permeation at 300 and 1600 ps

C coverage (Fig. 3b, 1600 ps), much reconstruction of the iron surfaces was observed; many carbon atoms have permeated into the surfaces. In particular, the surfaces of (111), (211), and (310) are not even flat anymore, but shows some wrinkles. Also, at this stage, the surface is mostly covered by graphitic carbon, in agreement with experimental studies from Sasol [8].

To quantitatively measure the degree of surface reconstruction at late stages of C permeation, we calculate the phase transitions related to the close packing of the Fe atoms due to carbon permeation after 1600 ps of MD simulation. Following the local crystalline classification visualized by Ackland-Jones bond-angle method [55], the close packing of each Fe atom was analyzed based on its separations from neighbor Fe atoms. The ratio of the Fe atoms in the slab models adopting different structural types are calculated and plotted in Fig. 4.

For both 300 K and 600 K (Fig. 4), the majority of the Fe atoms are still in a BCC-type close packing (Cyan bars). This is not a surprise, as the C atoms only penetrated into the several top layers on the surfaces even after 1600 ps of simulation; most of the Fe atoms in the deeper layers keep their
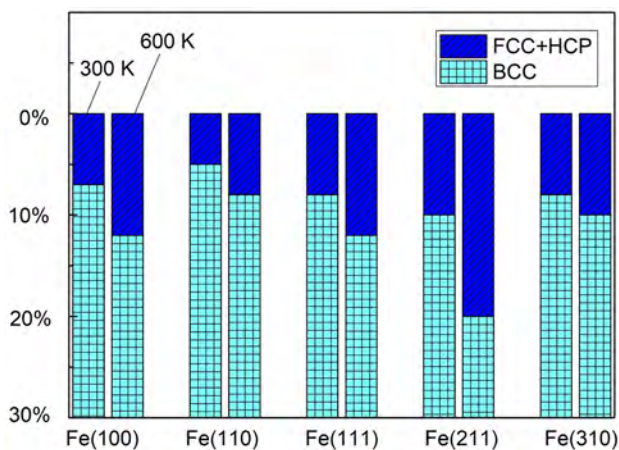
Fig. 4 The composition of new surface phases (FCC + HCP) on the five Fe surfaces at 300 K (left bar) and 600 K (right bar) from MD simulations

Fig. 5 $\Delta\mu_c$ (eV) as a function of the number of introduced carbon atoms per unit area (n_C/nm^2) for Fe (100), (110), (111), (310) and (211). The yellow–brown points represent the $\Delta\mu_c$ of C atoms in the 1L layer, red represent adding carbons in the 2L layer, and green in the 3L layer. For emphasis, the arrows under the (100) curve mark the critical branch points, at which the mode (layer) of permeation changes. The black dashed lines show the comparison in $\Delta\mu_c$ at the marked critical points, illustrating the energy difference for keeping a C in its layer and moving it to the next layer. From this point on, the lowest $\Delta\mu_c$ is chosen to extend the curve

crystalline structure. After further C permeation, the surface regions of the Fe lattice show two new crystal phases, FCC and HCP, with the ratio depending on the direction of the surface. These phases differ from pure bulk Fe, which exists solely as BCC, indicating that carbon permeation triggers reconstruction of the surface regions, which eventually leads to surface phase transitions. These new surface phases have strong correlation with bulk iron carbides phases, as the Fe atoms in both bulk Fe_5C_2 and Fe_3C are known to have distorted HCP close packing. In addition, as the temperature is switched from 300 to 600 K, the ratios of FCC and HCP in all five facets increase, indicating that temperature could accelerate the surface phase transitions.

In the light of the MD simulations, in the rest of this work, we separate the initial stages of C permeation from the overall carburization process, by assuming that the Fe surfaces are not destroyed much by the C permeation. With this simplification, we use DFT methods to study the nature of the early C permeation process and its correlation with FTS from several crucial perspectives.

6.1 Structures at Different Stages of Carbon Permeation from the Surface into Bulk

We began with an analysis of the thermodynamics associated with carbon atom adsorption on the surfaces of the Fe (100), (110), (111), (310), and (211) models. Many possible geometries of Fe surfaces with different surface carbon coverage were probed; the ones shown in Fig. S1–S5 are the local minima reached given the method of introduction of the carbon atoms into the system. The average carbon chemical potentials $\Delta\mu_C$ of these structures are plotted as a function of the number of adsorbed carbon atoms per unit area in Fig. 5.
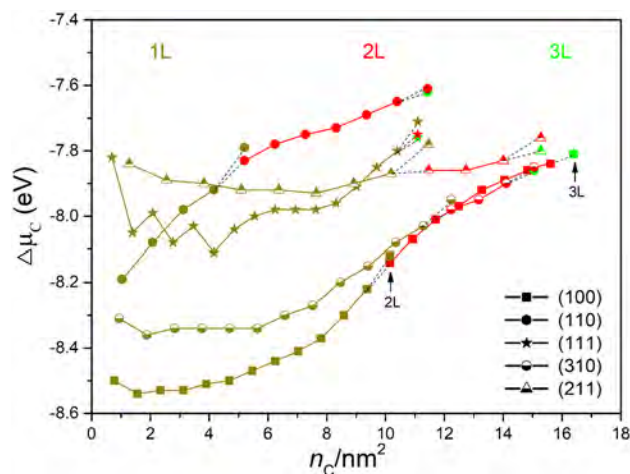
We assume that carburization occurs in the following sequence: when there are only a few C atoms adsorbed, only the 1st layer of Fe is carburized; eventually, as more C atoms are introduced, the carbon atoms may permeate subsurface. Another way to describe this second stage is to say that the 1st and 2nd Fe layers are carburized simultaneously, and so on. Consistent with this idea, before the carburization of the next layer commences, a critical value of the total number of C atoms per unit area introduced on or in the given layer is reached. As we add further carbon atoms to the surface, the magnitude of the binding energy per added C ($\Delta\mu_C$) increases or decreases, as indicated by the first layer (1L) curves (yellow–brown) in Fig. 5. At some point, for instance on the (110) surface when the 5th carbon atom is added, the average binding energy between the C atom and the slab becomes smaller in magnitude when the added C atom is in the original surface (1L) layer, compared to its optimal position when it enters the next layer (2L). Sometimes the difference in $\Delta\mu_C$ at the critical points (the average energy of adding the C atom to the current layer compared to adding it to the next layer) can be very small (a few meV). In the case of (100) surface, the $\Delta\mu_C$ is almost the same between 2L and 3L. But as long as the $\Delta\mu_C$ of the next layer is equal or smaller than that of addition to the present layer, we assume this is an indication of the inception of permeation into the next layer thermodynamically; the kinetics are explored below.

From this point on (we call it a critical branch point), the subsequent carbon atoms added to the array may go subsurface. Now the energies evolve along a new curve, which we label 2L (red). Upon addition of further carbons, the magnitudes of the binding energies decrease again in a smooth way, until another critical branch point, at which the $\Delta\mu_C$ indicates preference of C permeation into the next lower layer. At this point a certain atom enters the third layer (3L, green). Our exploration of systematic carbon permeation terminated when a C atom entered the 3L, as we assume that subsequent, deeper carbon penetration is comparable to carbon diffusion in the bulk of Fe crystal. The deposition of C atoms with very high coverage is known to form graphite layers/islands [56, 57], and is out of the scope of this study. The (111) surface is slightly different from others: after the 1L is filled, it was found that there is an energetic preference to put the next C atom directly in 3L, rather than in 2L.

An important limitation of these studies must be mentioned: all the structures shown are local minima reached by the specified sequential processes of "shooting in" C atoms, and letting them find the optimum site by a single geometrical optimization. Should there be a lower energy geometry that can be reached by overcoming an activation energy, our optimization process will not find it. In a subsequent paper, we will use a minima-hopping structural search to access just those geometries.

The equilibrium structures of layers in which the first carbon atom is adsorbed at the surface, 1L (corresponding to the beginning points of the curves in Fig. 5), and those penetrating to subsurface 2L and 3L (corresponding to the branching points of the curves in Fig. 5) on the five facets are shown in Fig. 6. In Fig. 6 we show only the beginning stages of permeation—for 1L, 2L and 3L only the first geometry for which one atom has entered the respective layer. These stages are marked by an arrow for the (100) surface in Fig. 5, the average binding energy diagram. We will now use the (100) surface case to illustrate the detailed mechanism of C permeation.

As Fig. 6 shows, the first C atom prefers to enter a fourfold hollow site in the 1L of the Fe (100) surface, a typical chemisorption site. This bonding geometry has been observed in scanning tunneling microscopy (STM) experiments [18]. Further carbon atoms (up to 12 in total for this surface cell) come in mostly along diagonal directions relative to the first chemisorbed C. The tendency to separation between the C atoms on the (100) surface has also been confirmed in the STM experiments [18]. At this point, the binding energy of the 13th C atom becomes less favorable in the 1L than the 2L layer by about 0.2 eV (difference in $\Delta\mu_c$ of 0.02 eV). Proceeding in this way, we find that the 2L layer can accommodate 8C atoms before C atoms enter the 3L layer.
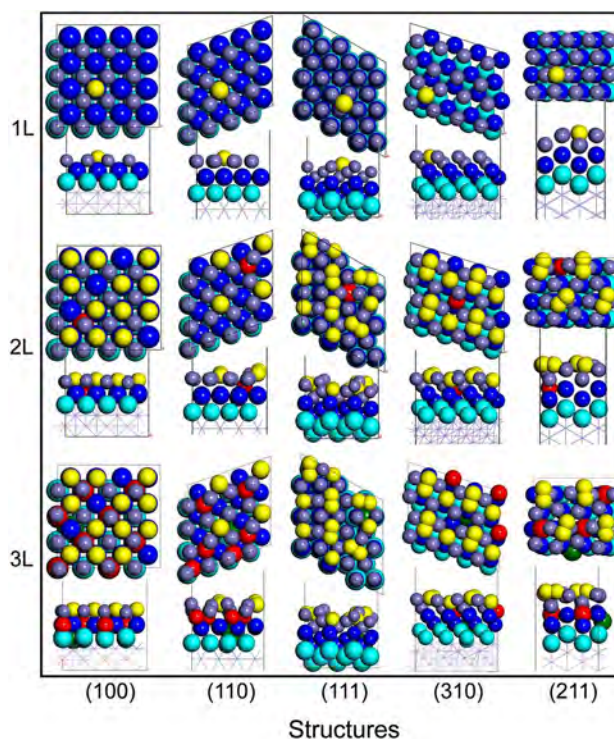

Fig. 6 The top and side view of optimized structures with the first carbon atom adsorbed on the 1L (surface) layer (in yellow), penetrating to the 2L layer (in red), and to the 3L (in green) on the five facets of Fe studied. The colors used are chosen to be consistent with the colors of the 1L, 2L, and 3L curves in Fig. 5. The 1st, 2nd and 3rd Fe atom layers are given in grayish blue, dark blue and cyan, respectively. We use spheres of slightly different sizes to represent the Fe atoms in different layers (1st < 2nd < 3rd), so that the embedded C atoms can be easier seen

The position of the critical branch points (marked by the arrows) in Fig. 5 indicates that carburization of Fe depends on the type of surface. On (110), introducing more than 6C atoms per nm^2 leads to calculated carburization of the second layer, while on (310), 13C atoms per nm^2 are needed. The initial carbon penetration to 3L on Fe (110) and (111) occurs at relatively low carbon coverage ($11C/nm^2$), carbon permeation to 3L on Fe (310) occurs at medium coverage ($15C/nm^2$), whereas carbon permeation to 3L on Fe (211) and (100) occurs at high carbon coverage ($17C/nm^2$).

7 Dicarbon

On three of the surfaces—(111), (310), and (211)—we see a striking phenomenon, the formation of C_2 dimer units, also called dicarbon. The dimerization of C atoms on the Fe (111) surface was found previously by Nieminen et al. [58]. In our calculations, C_2 dimerization first happens when 10 carbon atoms are added on the (111) surface, 3 carbon atoms on (211), and 9 carbon atoms on (310).

The C_2 molecule in the gas phase has in its ground state an equilibrium distance of 1.24 Å, and has a multitude of well-characterized excited state, some low-lying, with generally longer bonds. The bonding in C_2 has been the subject of much discussion [59].

The C–C bond lengths calculated for the chemisorbed C_2 units depend on the surfaces. On (211) and (310), the C–C bond length is typically 1.34–1.36 Å, in the range of C=C double bonds. On (111), the C–C bond length is slightly longer (1.39–1.45 Å). There is precedent for chemisorbed C_2. It has been reported in a theoretical study [60] that the two carbon atoms adsorbed on Ni (111) surface prefer to form C_2 dimer units (rather than separated C adatoms) by over 0.21 eV. Experimentally, on Ag (110) surfaces, C_2 dimers (bidentate acetylides, in the nomenclature [61]) can be stable up to 550 K, before dissociating to separate C adatoms. The C–C bond length on Ni (111) is 1.33–1.34 Å, slightly smaller than the C–C distance of C_2 on Fe (111) surface. In discrete molecules one finds another class of substances with C_2 units: dicarbide molecular clusters. Examples are $CpFeRu_6(\mu_5\text{-}C_2)(\mu_5\text{-}C_2H)(CO)_{16}$ [62] and [PPN] $[Fe_3Co_3(C_2)(CO)_{18}]$ [63] complexes. In these molecules, the C–C bond length varies between 1.33 Å and 1.42 Å, similar to what we computed for the C_2 units on the Fe surfaces in this study.

In our calculations, the coordination of the C_2 units on Fe surfaces usually involves 5–7 Fe atoms (Fig. 7), with the C_2 units sitting on top of an Fe atom in a slightly lower level, while also interacting with the other 4–6 Fe atoms at the same level. (310) is an exception, for it does not involve an Fe atom below the C_2 units. The C–Fe distances of about 2 Å in the surface- coordinated C_2 units are typical of C–Fe distances in numerous organometallics [62–65]. On average, the C–Fe bonds from C to the second layer Fe (on which the C_2 units are sitting on top) is longer than the C–Fe bond
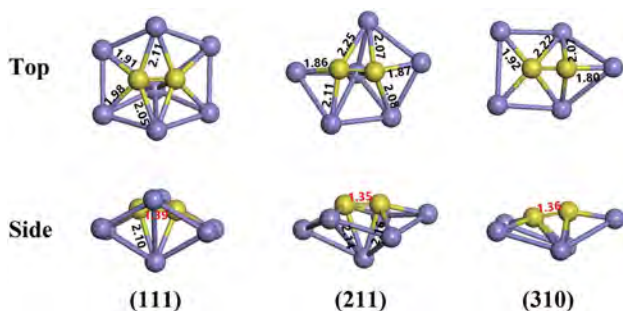

Fig. 7 Some coordination environments of the computed chemisorbed C_2 units on different Fe surfaces. The grayish spheres are Fe atoms and the yellow spheres are C atoms. The C–Fe bond lengths (labeled as black) from the C atoms to the same level Fe atoms are marked in the top views; the C–Fe bond lengths from C to the lower level Fe atoms (labeled as black) and the C–C bond lengths (labeled as red) are marked in the side views. All distances are in Å

from C to the first layer Fe by about 0.1 Å. The bonding of the Fe atoms to the C_2 units clearly has both σ and π components. The chemisorbed C_2 units are interesting, for they have the potential of serving as precursors for the formation of large aromatic carbon materials such as carbon nanotubes or polycyclic aromatics. And the C_2 units might be directly observable with STM.

We checked whether longer C_n chains might form on Fe surfaces at low carbon coverage. For C_3, all models proved unstable with respect to fragmentation to $C_2 + C$. However, at higher C coverage eventually graphitic layers do form.

7.1 Initial Chemisorption—the First Carbon on the Surface

Let's next focus on the thermodynamics of permeation. As defined in the methods section, the average carbon chemical potential ($\Delta\mu_c$) was calculated via the equation $\Delta\mu_c = (E_{nC/slab} - E_{slab})/n - E_C$, in which $\Delta\mu_c$ is defined as a function of the number of deposited carbon atoms per unit area (n_c/nm^2) (see Fig. 5). $\Delta\mu_c$ thus can be interpreted as a measure of the average C atom binding energy of all the C atoms hitherto introduced to the slab: the more negative the $\Delta\mu_c$ values is, the more is the C-permeated structure energetically favorable for a C atom.

At the lowest coverage ($n_c/nm^2 = 0$), $\Delta\mu_c$ on the five facets follows the order (100) < (310) < (110) < (211) < (111), reflecting the finding that the Fe (100) and (310) surfaces are initially more favorable for carbon adsorption than the (111) and (211) surfaces. Here, we investigate the situation where only one carbon atom is adsorbed on the surfaces, to try to understand the above trend. The $\Delta\mu_c$ in this case reduces to simply the adsorption energy of the carbon atom ($E_{ad} = E_{C/slab} - E_{slab} - E_C$). The adsorption energies correspond to the first entry at left in Fig. 5. These range between −7.8 and −8.5 eV. This energy range is in consistent with previous studies, where C adsorption energy is −8.35 eV [58] and −8.33 eV [25] on (100), −7.98 eV [58] and −7.97 eV [27] on (110), and on −7.74 eV [58] on (111). In our study it is −8.50 eV on (100), −8.19 eV on (110), and −7.82 eV on (111).

Why is there such a pronounced difference in chemisorption of C on different Fe surfaces? Perhaps the surfaces are predisposed to bond C better or worse, even if the energy is lowered on chemisorption. A Pauling bond order (PBO) [66] is an empirical measure of the strength of bonding interactions, originally suggested by Pauling in 1947. For any bond, its PBO is defined as $n_x = n_0 EXP((r_0 - r_x)/c)$, where n_x is the bond of length r_x with a reference bond length r_o, and c (0.3) is a constant that determines how steeply the bond order change with bond distances. Here, we use a typical Fe–C bond distance ($r_0 = 1.938$ Å) of a carbon atom adsorbed on the Fe (100) surface as a reference bond with
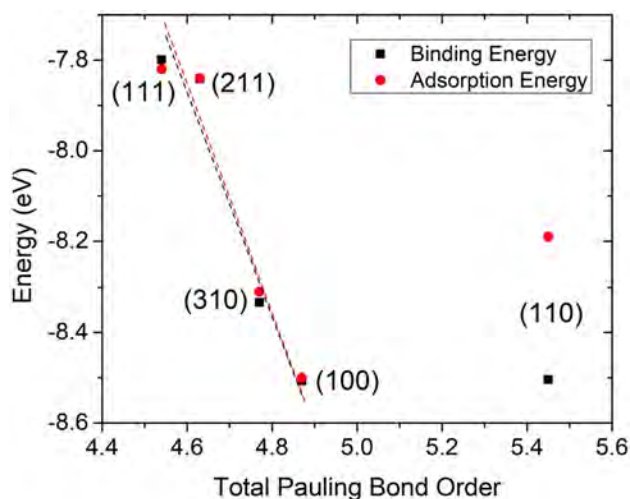
Fig. 8 The correlation of the carbon adsorption energy (red spheres) and binding energy (black squares) of the five surfaces with the total PBO of the C–Fe bonds
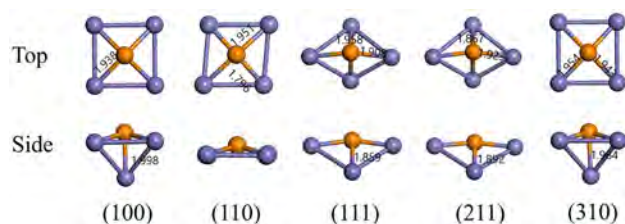

Fig. 9 The top and side view of the C–Fe bonds with more than 5% contribution to the total PBO in the adsorption of a C atom (brown) on the five Fe (grayish blue) surfaces. The units of the (C–Fe) bond lengths are Å

$n_0 = 1.0$. Looking for a correlation between adsorption and C–Fe bonding strength, for each surface, the carbon atom adsorption energy was plotted vs. the sum of the PBOs between the C atom and the Fe atoms surrounding it.

As Fig. 8 shows, one can see a rough correlation between the adsorption energies (red points) and Pauling bond orders for four of the five surfaces. The fifth, the (110) surface, is way off. Its binding of C is intermediate, but there is a large PBO attached. We thought surface relaxation might be at work, so we repeated the correlation, now relaxing each surface (black points, the binding energy $E_{bind} = E_{C/slab} - E_{slab\_bind} - E_C$, where E_{slab_bind} is the energy of the slab at the prepared geometry for binding the C atom). As the figure suggests, only the (110) surface relaxed substantially. But this surface still eludes correlation with the others. We then decided to look at structural details in the surfaces.

In Fig. 9, we show the structures of the bonded surface complexes with all the C–Fe bonds that contribute at least

5% to the total PBO. The (110) surface binds the C atom in a rhomboid geometry. There is another Fe atom below the C atom. However, the C–Fe distance is rather long (2.341 Å), contributing very little to the total PBO (less than 5%), and is not shown in the figure. The (110) surface is distinguished by two very short C–Fe bonds with length of only 1.796 Å, considerably shorter than the C–Fe bond lengths in any other surfaces. Since a PBO is an exponential function of the bond length, these two short bonds cause the total PBO of the (110) surface to be substantially larger than that of others.

Radio frequency plasma discharge studies have shown some time ago that C deposition on iron surfaces is a result of the catalytic activities of the exposed surfaces [67]. But why does the C atom bind more strongly with three of the surfaces (100), (110) and (310) rather than the other two (111) and (211)? From Fig. 9, one immediately sees the square planar (or nearly such) disposition of four ions around C in these surfaces; as we mentioned above, there is actually a fifth carbon atom some distance further away, at the apex of a square pyramid. The carbon atoms in these CFe₄ units are only slightly above the Fe₄ plane (0.4 Å above the mean plane for the (100) surface.) These surface carbide structures show a distinct geometric feature, a rotation of the top layer relative to underlying ones, for which Nandula et al. [68] identified (for CCo₄ and CNi₄) a special electronic stabilization for analogous carbides. The extra stability of these units was traced to a unique π-state where two electrons are localized over a single square. Perhaps a similar stabilization is at work for the iron surfaces; we will explore this in the future.

7.2 Sequential Chemisorption; a Role for Charging and Coordination Number

As the surface carbon coverage increases, both Fe (100) and (310) models feature an initial slow and subsequent faster rise of $\Delta\mu_c$, from -8.4 to -7.8 eV. However, Fe (110) displays a very fast rise of $\Delta\mu_c$. Despite the $\Delta\mu_c$ for the Fe (111) models showing a jagged chemisorption energy profile (which we are trying to understand), the $\Delta\mu_c$ of both Fe (111) and (211) doesn't change drastically with increased surface carbon coverage.

There could be electronic and geometric reasons for the change of $\Delta\mu_c$ with coverage. Electronically, as C atoms are added to the Fe surfaces, there will be electron redistribution from Fe to C atoms, to form a carbide (with oxidation of Fe). With an increase in the number of C atoms, the average effective positive charge [69] of Fe should increase. We decided to use the Bader partitioning to define a charge at each Fe or C atom. The effect mentioned can be clearly seen in Fig. 10, using the (100) surface as an example—as the number of C atoms increases, the Fe atoms become more positive.
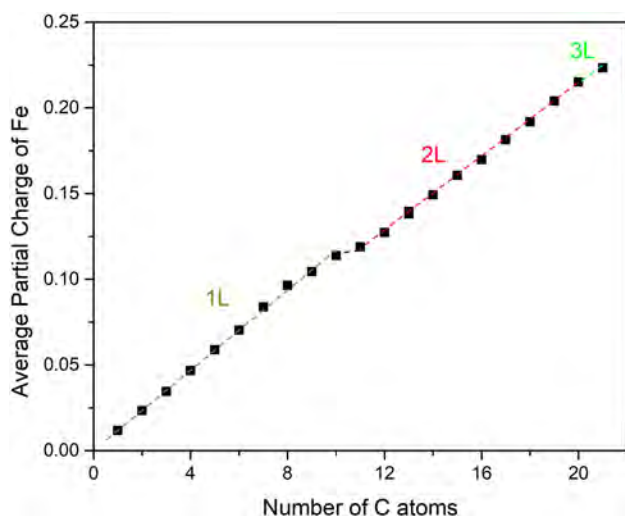
Fig. 10 The change of the average partial charges of the 96 Fe atoms in the (100) surface slab as a function of the number of C atoms on/into it (1L carbon in yellow–brown; 2L carbon in red, and 3L carbon in green)

In exploring the effect of "charging" on chemisorption energetics, the extension of the 1L curve does not overlay with the 2L and 3L curve, because of the different chemical environment of the C atoms on the surface and in the bulk. So the Fe atoms' resistance to further electron transfer to C coming on the surface will increase. This should make the carburization process more difficult with increase of the number of C atoms, as our calculations indicate in general. Our calculation is also in agreement with a previous X-ray photoelectron spectroscopy study [56]. The C 1s binding energy of the chemisorbed C on the Fe (100) surface (corresponding to the 1L layer in our study) shifted to lower binding energies by 0.7–1.1 eV compared to the C in the carbide bulk phase (corresponding to the 2L and 3L in our study), showing a stronger charge transfer from Fe to C atoms for chemisorbed C than for C in the bulk phase.

A second reason for change in C chemisorption energy might be the higher affinity of the C atom for low coordination surface Fe atoms compared to the generally higher coordination subsurface Fe atoms. To probe this effect, we placed a C atom deep subsurface (in 3L) and optimized its structure. For example, on the (111) surface slab, putting a C atom on the surface is more stabilizing than putting it deep in subsurface (at 3L) by about 0.5 eV. Because of these electronic reasons, we see a generally increasing $\Delta\mu_c$ curve (a smaller magnitude of the binding energy) in Fig. 5.

However, relaxation of the structures of the surfaces upon carbon permeation, which depends on the topology of the specific surface (and is hard to predict), also is likely to play a role, and makes the $\Delta\mu_c$ curves look jagged. The most irregularly shaped curve in Fig. 5, the (111) surface curve,

is probably such because of strong surface relaxation effects, as we can rule out two electronic factors (C–Fe coordination number and the effective charge on Fe). As one adds C atoms (from 1 to 10), the C atoms all prefer to be separated on the surface. Therefore, the coordination number of C does not change. The average effective charge of Fe will also keep increasing. However, in Fig. 5, we still see a very rough (111) $\Delta\mu_c$ curve, with ups and downs, in this region of carbon coverage.

We mention again a limitation of this stage of our study—our optimization leads only to the local minimum reached in a barrierless process for a given surface and coverage. We will explore the global minima, attained in a finite T model of the FTS reaction, in subsequent work.

At a high coverage ($n_c/nm^2 = 11$), carbon adsorption remains favored on Fe (100) and (310) compared to other surfaces, and the $\Delta\mu_c$ order becomes (100) = (310) < (211) < (111) < (110). High $\Delta\mu_c$ (smaller binding) at high coverage indicates that when the upper layers are occupied, the lower layers have a smaller (in magnitude) binding energy as more C comes in. One might imagine that if there is a barrier for the diffusion of an upper layer C to lower layers on (110), that the upper layer C atoms would serve to protect the lower layer from being further carburized. However, we will see from the transition state calculations in the next sections that this is not the case: the carbon atoms in the upper layers of a (110) surface have a rather low barrier of diffusion into deeper layers.

The reader will notice that the average binding energy per atom decreases in magnitude (less so for the (211) surface) with increasing carburization. It appears that entrance of carbon atoms subsurface is accompanied by a smaller magnitude of stabilization than their chemisorption on top of the surface. This is consistent with the result mentioned above that inserting a single carbon atom into the interior of a 3-layer model of bulk Fe, re-optimizing the structure, we get a $\Delta\mu_c$ of -7.28 eV, substantially smaller in magnitude than all the points in Fig. 5.

7.3 Detailed Reaction Paths for Difficult and Easy Permeation

To understand the kinetics associated with carbon permeation, migrations of carbon atoms along the direction roughly perpendicular to the surface were investigated on the five facets. As shown in Fig. 5, the critical branch points at which the incoming C atom prefers to go into a deeper layer rather than staying in the current layer are marked by branching dashed lines. To get a microscopic picture of what exactly transpires in permeation, we look in more detail at reaction paths for migration just at these branch points. At the critical branch point in Fig. 5, the upper branch geometry (the state in which the C remains in its present layer) is set as
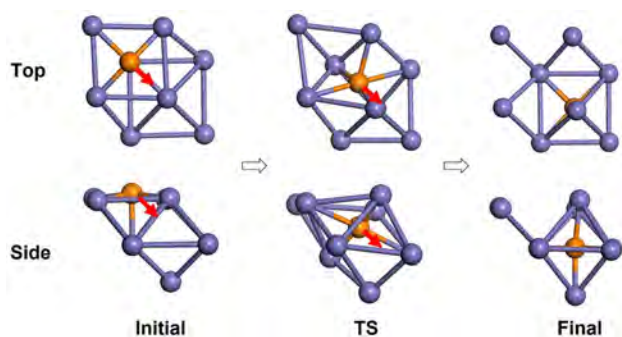
Fig. 11 Top and side views of the migration of a carbon atom from the surface (1L) to the second layer (2L) on Fe (100). The C atoms are in orange and the Fe atoms are in grayish blue. The motion of the carbon is indicated in red
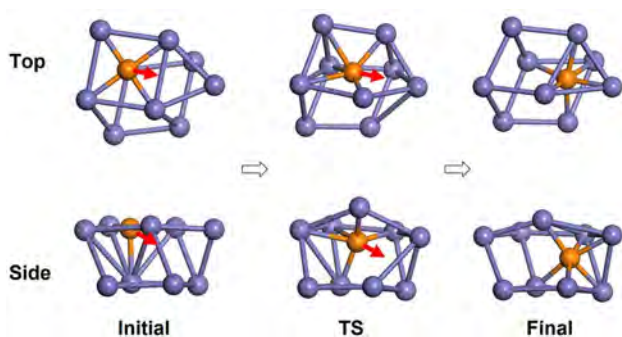

Fig. 12 Top and side views of the migration of a carbon atom from the surface (1L) to the second layer (2L) on Fe (110). The C atoms are in orange and the Fe atoms are in grayish blue. Red arrows indicate C atom motions

the initial state, and the lower branch (the state in which the same C moves to a deeper layer) is set as the final one. Geometrical transitions and migration barriers between these initial and final states were calculated with the NEB method.

We start with the study of the transition from 1L to 2L. As Fig. 5 shows, the total number of carbon atoms at the branch critical points for 1L to 2L transition are 13, 5, 16, 13 and 9 for the Fe (100), (110), (111), (310) and (211) surfaces, respectively. We will use the motion of a C atom from 1L of a (100) and a (110) surface model to 2L (Figs. 11, 12) as examples. It is not easy to show the complex motion of both Fe and C atoms in the course of this first stage of permeation, but perhaps in the absence of a movie of a reaction itinerary, we may approach visualization via three snapshots (initial geometry, transition state and final one) in top and side views. The moving C is in orange, with its motion marked by a red arrow.

In the side view of Fig. 11, one can clearly see that the C atom slides down from 1L to 2L, bypassing the Fe atom beneath it. The top view shows that the C atoms also move along the diagonal direction of the surrounding Fe_4 square.

The migration starts with a five-fold coordination of C (four Fe atoms on surface, one underneath; the cutoff for showing an Fe–C bond is 2.2 Å). To get to the transition state, the C atoms has to move towards the diagonal direction of the Fe_4 square, where an Fe atom is located on the vertex of the square. In the transition state, the migrating C atom is located in a very distorted octahedral-like interstice, which involves stretching or local dilation of the 1L Fe_4 square (in a strongly bonding CFe_4 unit, as we discussed earlier) into a rhombus, and distorting one of the Fe atoms in the 2L Fe_4 square. Also, in the transition state the structure is so distorted that the distance from the C to the Fe beneath it becomes 1.695 Å, considerably smaller than a normal C–Fe bond length of 1.9–2.0 Å. In the final state, the C atom occupies a near-octahedral site at 2L, and the distorted Fe_4 squares at 1L and 2L are restored. The structural features noted for the TS suggest a high permeation barrier on the (100) surface, and indeed that is what is calculated (1.64 eV).

The barriers to permeation vary substantially, depending on the surface. C permeation on the (110) surface also starts with a five-fold coordination of the 1L C (four Fe atoms on surface, one underneath). However, the Fe_4 square is a somewhat rotated one with respect to the second layer Fe atoms. As a consequence, when the system transforms to the transition state for permeation, the C atoms only need to move along the dashed red arrow in the middle of the square, with potentially much smaller steric constraint (Fig. 12) than the case of (100) surface. As a result, in the transition state, only a relatively small distortion of the Fe_4 square is involved, where one of the Fe atoms in the corner is slightly "lifted up". In the final state, the C atom also occupies an octahedral-like site. Not much energy is needed to distort the structures of the surface region along the reaction, and a low permeation barrier is calculated as 0.27 eV. The existence of the permeated C atoms at the octahedral interstices in the carburized Fe surfaces has been confirmed experimentally by Mössbauer Spectroscopy; they have been termed as "O carbides" [70].

8 Permeation Will Vary Substantially with Surface

In Fig. 13, the calculated barriers estimated by the energy of (TS2) of carbon atom permeation in these five surfaces from 1L to 2L, 1.64 eV/Fe (100), 0.27 eV/Fe (110), 1.33 eV/Fe (111), 1.09 eV/Fe (310) and 0.70 eV/Fe (211), are compared. We have already looked in detail at the largest and smallest of these. The overall range of barriers is substantial; while we don't take the absolute numbers seriously, the variation observed is surprising, and very likely relevant for catalysis.
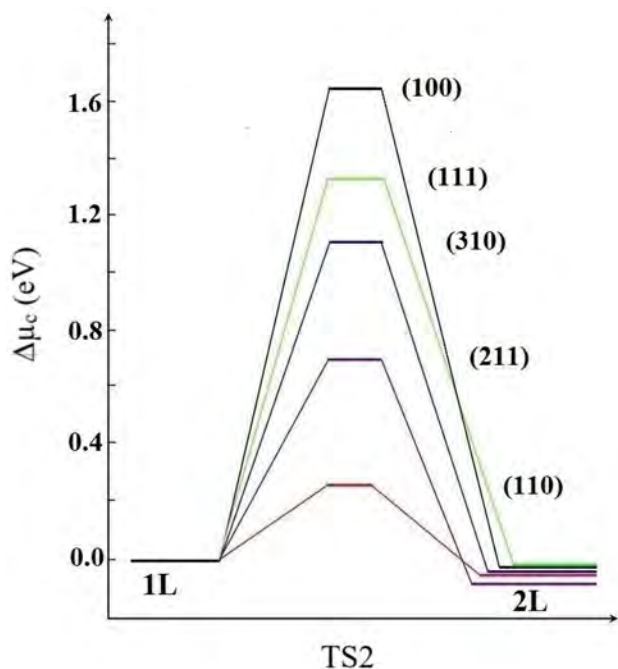
Fig. 13 Energy profiles of carbon atom permeation from the surface (1L) to the second layer (2L) on Fe (100), (110), (111), (310) and (211) surfaces

Fig. 14 Computed energy profiles of carbon atom permeation from the second layer (2L) to the third layer (3L) on Fe (100), (110), (111), (310) and (211) surfaces

We might think that the more "open" (or "rougher") surfaces such as (111), (211), and (310) will have lower permeation barrier than the more "compact" (or "flat") surfaces, (100) and (110). However, it turns out the (110) surface has the lowest calculated carbon permeation barrier in moving from 1L to 2L, while (100) is the surface with highest barrier. The barriers on the "open" surfaces of (111), (211), and (310) are in-between these two extremes. In fact, if we count the nearest neighbor, or coordination number (CN), of the topmost Fe atoms on the five surface, using the Fe–Fe bond length in bulk (< 2.45 Å $+ 0.05$ Å) as a criterion, then we have CN $= 4$, 6, 3, 5, 4 for (100), (110), (111), (211), and (310) surfaces, respectively. There is no direct correlation between the CN of the topmost Fe atoms on the surface, and the C permeation barriers.

As we have suggested, using the (100) and (110) examples above, the dominant factor behind the permeation barrier variability is likely to be found in the different stacking geometries of the Fe layers on the different surfaces. This in turn causes one surface to have a more favorable permeation pathway than another one, from the surface adsorption site down to the octahedral-like interstitial sites in the bulk. The details are difficult to unravel, though we have attempted to do so in the two cases illustrated.

In an analogous way we studied the permeation of C from 2L to 3L; the computed barriers (TS3) are shown in Fig. 14. Again, the (110) surface has the lowest 2L to 3L C permeation barrier, while (100) has the largest one. Clearly,
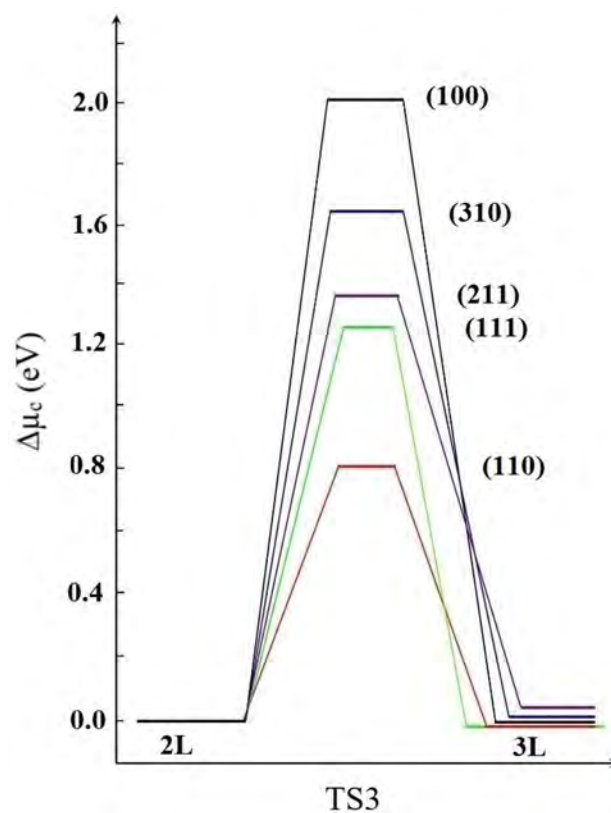
permeation 2L to 3L encounters higher barriers than 1L to 2L. This is not hard to understand. As Fig. 2 shows, the surfaces are periodically stacked structures, with similar structures among the layers (for 111, 211, and 310, we consider multiple sublayers as one layer). Because the 1st layer Fe atoms at the solid–vacuum interface have fewer nearest-neighbors than the Fe atoms in other layers, they have more freedom of motion; we imagine it is easier to distort the surrounding Fe atoms to "open up" a path for C to permeate, making the permeation from 1L to 2L easier than from 2L to 3L.

9 Permeation vs Surface Migration

At the branch critical points, the neighboring sites of the permeating C atoms in most cases are already occupied by other C atoms, so it would not be likely that the permeating C atoms would be free to migrate on the surface. However, a question one could ask is: given similar kinetic energy (provided by the temperature) for the systems to cross various barriers available to them, would some C atoms migrate on the surface, while other C atoms penetrate into deeper

layers? To provide some input on this question, we calculated the migration barriers of a C atom (not the C at the critical branch point, but a C atom with available neighbor adsorption sites at lower C coverage) on the five surfaces, and compared the surface migration barriers to the migration barriers for penetrating subsurface of the C at the branching critical point (1L–2L).

Because of the possible formation of C_2 units on some of the surfaces, surface migration can be quite complicated. For instance, the following situations are all possible: (1) isolated chemisorbed C migration on the surface, (2) $C + C \rightarrow C_2$, (3) an exchange reaction with a chemisorbed C_2, $C + C_2 \rightarrow C_2 + C$, (4) C_2 migrating as a unit, and (5) C_2 breaking up, one C going subsurface and one remaining on the surface, etc. For simplicity, here we only consider the first possibility,—the migration of a C atom on clean surfaces that are covered only by one C atom.

As shown in Fig. 15, on most of the surfaces studied, the surface migration barrier on clean surfaces (cyan bars) is larger than the permeation barriers (green bars). The (111) surface seems to be an exception, with a slightly smaller surface migration barrier. In general, it seems that surface migrations on clean surfaces should be harder than permeation at the branch critical points, except for the (111) surface.

We also examined C migration on surfaces covered by C to a greater extent (yellow bars). When the C coverage increases to intermediate (with 13, 5, 16, 9, 13C atoms on the five surfaces, respectively), all the surface migration barriers change, with the barrier on (100), (110), and (111) surfaces going down, and those on (211) and (310) surfaces going up. In particular, the C migration barrier on the C-covered (100) surface drops substantially, and becomes much
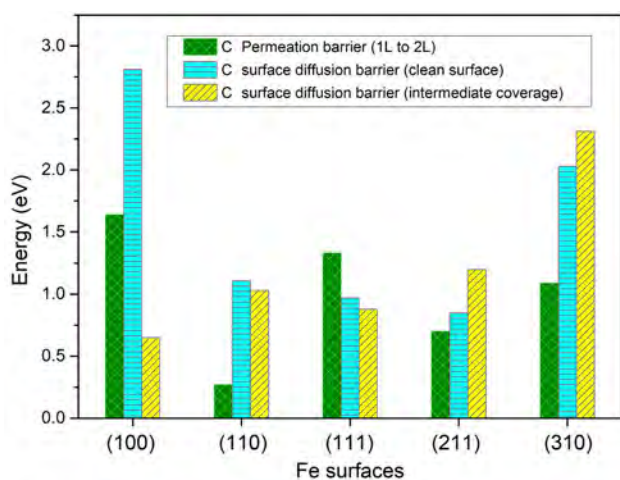
easier than permeation. From these comparison, we get an overall picture that although C permeation is preferred on many surfaces, surface migration of C also might be happening on some surfaces during the C deposition process.

10 Rate Constant Estimates for Permeation

The calculated rate constants for permeation (Table 1) at 600 K (using Eq. 1) naturally follow the barriers. The rate constants were calculated by using Eqs. (1) and (2) in the methods and models section, with the activation energies of Fig. 13. The rate constant of C permeation on the (110) surface is computed to be larger than that on the other surfaces by 7 orders of magnitude from 1L to 2L, and 4 orders of magnitude from 2L to 3L. The order of rate constant ((110) > (211) > (111) > (310) > (100)) from 2L to 3L emerges as being almost inversely correlated with the order of average binding energy $|\Delta\mu_c|$ at high coverage ((110) < (111) = (211) = (310) = (100)). Permeation on the (110) surface is most facile kinetically, but least preferred thermodynamically. This suggests that carburization on the various Fe surfaces is a process with opposite kinetic and thermodynamic preferences.

10.1 Morphological Evolution of Fe Nanoparticles on Carbon Permeation

The thermodynamic and kinetic investigations described above provide qualitative and quantitative information of the carburization process at various surfaces of Fe-based FTS catalysts. In practice, the catalyst morphology changes throughout the reaction. We are not yet in a position to study theoretically the complete evolution of a clean iron surface to a bulk carbide, but we can approach the problem by looking at the effect of carburization on the morphology of Fe nanoparticles. Such nanoparticles have been seen implicated in several studies [34, 71, 72].

The classic Wulff construction method is an effective tool in predicting the equilibrium structure of nanoparticles with

Fig. 15 The energy barriers of a carbon atom at critical branch point permeating from 1L to 2L (green bars), compared with the barriers of a carbon atom migrating on a clean surface (cyan bars) and one with intermediate C coverage (yellow bars, coverage specified in text)

Table 1 Barrier E_a (eV) and rate constant k (s^{-1}) of C transfer on Fe surfaces at 600 K

Surface	C transferring from 1st to 2nd layer		C transferring from 2nd to 3rd layer	
	E_a	k	E_a	k
Fe (100)	1.64	3.16×10^{-1}	2.01	3.32×10^{-4}
Fe (110)	0.27	2.56×10^{15}	0.81	1.26×10^{6}
Fe (111)	1.33	9.99×10^{1}	1.26	5.72×10^{2}
Fe (310)	1.09	2.58×10^{3}	1.64	2.13×10^{-1}
Fe (211)	0.70	7.37×10^{6}	1.35	4.21×10^{2}

defined morphology for a given catalyst [37, 51, 73, 74]. In particular, the equilibrium shape favors larger exposed areas for those surfaces with smaller surface energies, in order to minimize the overall surface free energy of the particle. Although the shape of Wulff construction depends on the size of the nanoparticle for small particles, it is independent of size when the particle size passes some critical value. Here we focus only on large particles.

The surface energies of five facets/surfaces of Fe were calculated using DFT methods (computational details in the methods and model section, calculated surface energies in SI). Let us assume that the five surfaces are in equilibrium with the same carbon reservoir with a specified carbon potential, $\Delta\mu_c$. The variations in surface energies (see Fig. S6 in SI) indicate that starting with clean iron surfaces, when $\Delta\mu_c$ is at -8.4 eV, only the (100) surface should show C deposition. As $\Delta\mu_c$ goes up to -8.2 eV, both (310) and (100) will have C atoms deposited on them. At higher $\Delta\mu_c$, all the surfaces should show C deposition.

The deposition of C atoms on the surfaces will naturally affect their surface energies, and this variation is also calculated in Fig. S6 in SI. The changes with coverage are not large, but do make a difference. Using these surface energies, the evolution of the shape of a typical iron nanoparticle due to carbon permeation may be predicted from a Wulff constructions (Fig. 16). The contribution of each facet to the total morphology of the model catalyst at different $\Delta\mu_c$ values was carefully examined. For pure Fe, the low-index Fe (110) was calculated to be the most stable among the five clean surfaces, making the largest contribution to the total surface area (38%), followed by Fe (211) (31%), Fe (310) (22%), and Fe (100) (9%). The pure Fe nanoparticle morphology is predicted to be mostly made up of these four facets. As carbon coverage of the nanoparticle faces increases, changes occur in the areas of the facets exposed, but they are overall not large. Figure 16 shows the Wulff construction of the nanocrystal for $\Delta\mu_c$ -8.2 eV, the SI shows other values.
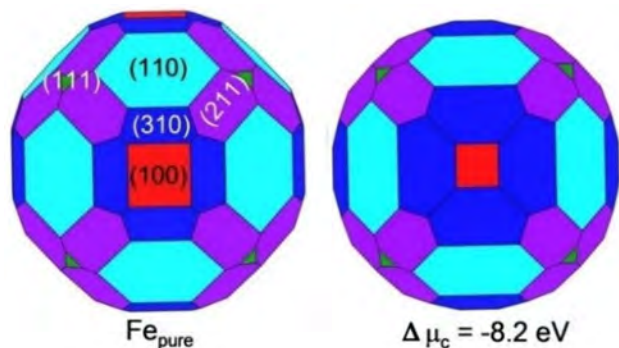

Fig. 16 The equilibrium morphologies of pure Fe and carburized Fe (at $\Delta\mu_c$ -8.2 eV) model clusters determined by DFT calculations, followed by Wulff constructions

How do these morphologies compare to experiments? The comparison is not an easy one to make. In experiment, for successful imaging, the nanoparticles are usually reported as supported ones. Since supported nanoparticles on foreign substrate follows a different set of physical constraints [75] to isolated ones [76], and the equilibrium shape of the former depends on the binding affinity of the nanoparticle with the substrate, the shape of our DFT-predicted Fe nanoparticles in vacuum cannot be compared directly with experiments. Also, the shape of synthesized metal nanoparticles depends strongly on the type of solvent used during synthesis [77], which is actually one of the important ways of controlling the shape of nanoparticles. Thus the shape observed may not be the most thermodynamically stable shape in vacuum.

In one case, large Fe nanoparticles supported on a Co/W (110) surface were found to expose only the (110) and (100) surfaces [78, 79]. Although the shapes (and therefore ratio of facets seen) of the nanoparticles differed among the ones observed in the experiment, one of the 7 nm pure Fe nanoparticle is estimated to expose 17% of its area with (100) and the rest 83% with (110) from the STM images [79]. This discrepancy between calculation and experiment is not a surprise, for reasons explained earlier. Other smaller Fe nanoparticles, of about 4 nm in diameter, expose also some facets of higher Miller indices, such as (221) and (211), but their area ratio cannot be determined from the reported images.

We have found only one experimental study of the shape evolution of pure Fe nanoparticles to carburized Fe nanoparticles [34]. The observation in this paper is that during the course of the experiment, the shape of the nanoparticle did not change markedly because of carburization.

In summary, the surface energy calculations and the Wulff constructions based on them (Fig. 16 and SI) indicate that the shape of the Fe nanoparticles and the ratio of exposed facets can be affected and modulated upon carbon permeation. The effect, although not dramatic, provides another possible mechanism for the change of shape of Fe nanocatalysts in FTS conditions.

10.2 Carbon Permeation Makes the Fe Surfaces Resemble Carbide Phases in Electronic Structure

Investigation of the d-band centers [80] of the carburized Fe facets provides insight into the influence of carbon permeation on the catalytic activity related electronic properties. In the d-band model of Nørskov [80, 81] and co-workers, the interaction of adsorbate molecules with metal surfaces is simplified to the interaction between the d-projected density of states (PDOS) with the molecular orbitals (MOs) of the molecules. The d-band center is defined as ($\varepsilon = \varepsilon_d - E_F$);

here ε_d is the first moment of the metal d-band-PDOS, and is calculated as:

$$\varepsilon_d = \frac{\int_{-\infty}^{\infty} \eta_d(\varepsilon)\varepsilon\, d\varepsilon}{\int_{-\infty}^{\infty} \eta_d(\varepsilon)\, d\varepsilon},\qquad(3)$$

where $n_d(\varepsilon)$ is the d-projected DOS, and ε is the energy. E_F is the Fermi level. The calculated d-band centers ($\varepsilon = \varepsilon_d - E_F$) of the five surfaces for both carburized Fe surfaces and bulk iron carbides are plotted in Fig. 17a. In the case of the carburized Fe surfaces, the d-band centers of all five surfaces moves further away from the Fermi level as the carbon coverage increases. As carbon coverage grows, the d-band centers of the carburized Fe surface steadily approach those of bulk iron carbides. This is direct evidence that surface carburization can modulate the d-band centers of Fe catalysts, making those surfaces resemble bulk carbide phases electronically.

CO activation is usually believed to be the rate-limiting step in FTS, and is a good model reaction to understand catalyst activity in FTS. Another specific descriptor that was recently reported to have strong correlation with CO activation barrier in Fe-based FTS is the site-dependent charge of the involved surface Fe atoms [82]. It was found that the less positively charged the involved surface Fe atoms, the easier the CO activation. This descriptor (q_{Fe}) is essentially an indication of the local environment of the active site, and is calculated as the average charge of the surface Fe atoms that are directly bonded with the adsorbed CO molecules.

From Fig. 17b we can see that with the increase of C coverage, the q_{Fe} of the Fe atoms on the Fe (110) surface increases. According to the linear relationship found in literature, C permeation tend to passivate the Fe surface for CO activation, and decreases FTS activity. The Fe (110) surface with intermediate C permeation (5C/nm^2) has about the same q_{Fe} with those of χ-Fe$_5$C$_2$ surfaces that are reported in literature. This is an indication that Fe (110) surface with intermediate C permeation is likely to have equivalent activity in CO activation to χ-Fe$_5$C$_2$ surfaces.

10.3 Carbon Permeation Changes the F–T Selectivity of Iron Catalysts

One of the main goals in FTS is to achieve high selectivity of desired C$_5$+ products and reduce methane selectivity [83]. Given the key role of carbon permeation in modulating morphology and electronic properties of the catalysts, it is reasonable to suggest that carbon permeation may also affect the selectivity of the reactions in FTS. It is known that the product selectivity in FTS can be varied over a wide range, and product distribution is one of the key factors in FTS [84].
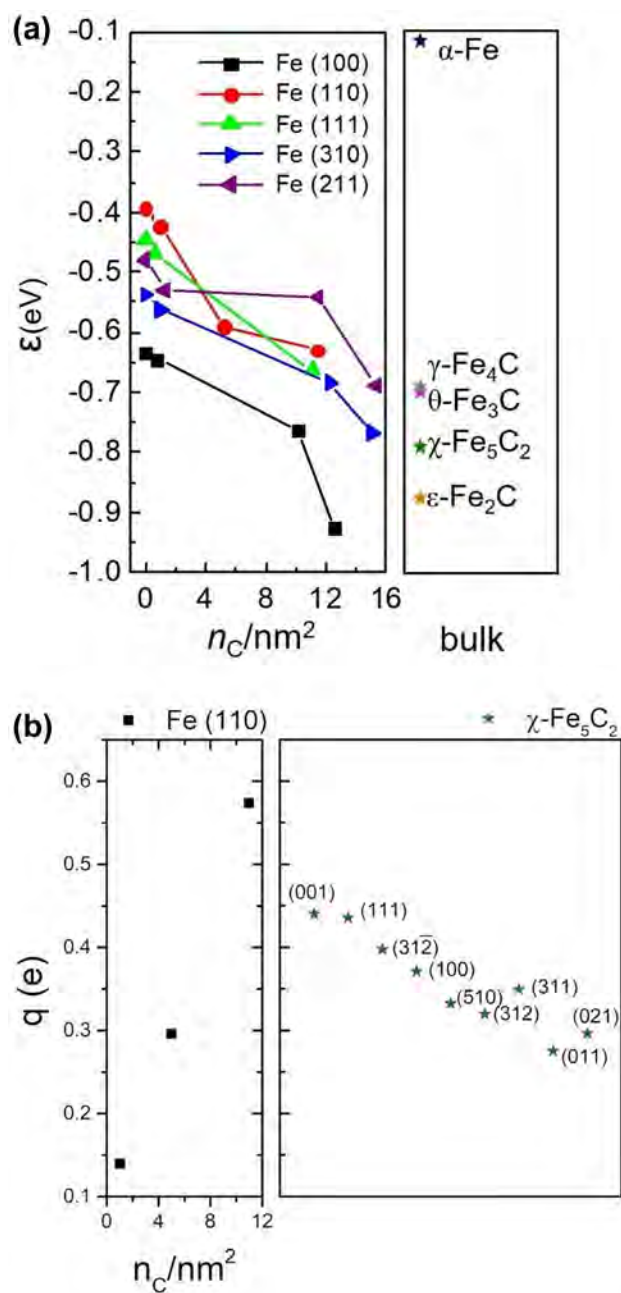

Fig. 17 a The d-band centers of the Fe surfaces at different carbon coverage (n$_c$/nm^2, lines) from DFT calculations; the d-band center of bulk iron and iron carbide phases are provided on the right side as references (stars). For all the systems, their corresponding Fermi levels were set as zero in d-band center. **b** The average Bader charge q of the involved surface Fe atoms for the CO activation for C permeated Fe (100) surface (left) and χ-Fe$_5$C$_2$ (right) reported in literature [82]

In FTS, there are several competing paths. Chain propagation by forming C–C bonds is the desirable path, leading to the formation of long chain hydrocarbons. Chain termination with methane formation is undesirable. We probe in a preliminary way how C permeation may affect the activity and selectivity of FTS by comparing the energy barriers of

two competing elementary reactions at different C permeation stages. The reaction barriers cited will be the energy differences between the TS and the initial reactant states (IS). The TS were located with the NEB method.

With CH_3 as an abundant surface species/intermediate in FTS reactions, two surface reactions of chemisorbed methyl were singled out for detailed study. First, we examine:

$$CH_3 + H \rightarrow CH_4, \tag{4}$$

the presumed rate-determining step of methane formation and a typical chain termination step [85–87]. Second, we look at a competing reaction:

$$CH_3 + C \rightarrow CCH_3. \tag{5}$$

Ethylidyne, CCH_3, is a well-known surface species; its formation is typical of CC chain extension.

Experimental studies from the Sasol group show that on both pure and surface-carburized Fe surfaces, the CH_s intermediate for methane formation and the CCH_s one for C2 hydrocarbon formation are the two most stable surface intermediates [8]. This supports the choice of the two reactions we have studied as representative enough to investigate the selectivity in FTS on Fe surfaces.

For both of the reactions, we take the same Fe (110) surface slab model as we used in the earlier sections. There are two reasons for choosing this surface. First, thermodynamic study shows that the critical branch point (the point at which chemisorbed C atoms begin to go subsurface) on this surface appears at relatively lower C coverage than other surfaces (Fig. 5). Second, our kinetic study indicated that this is the surface that is most susceptible to C permeation (Fig. 13). We start our comparison of the two reaction where altogether there is only 1C atom available on the surface (1C/supercell, Fig. 18a), dictated by the carbon chemical potential of the FTS environment. Note here that we want to compare the two reactions at the same carbon chemical potential. Therefore, for reaction (5), we don't provide a
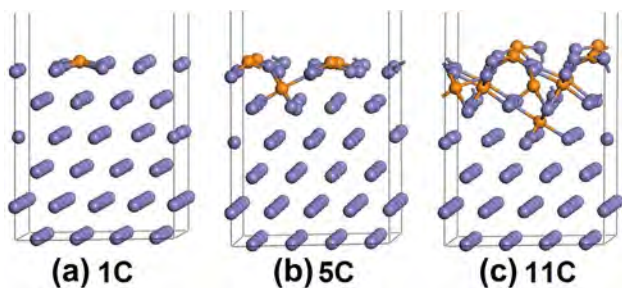

Fig. 19 Top and side views of a C–H coupling reaction on Fe (110) at C coverage of 1C. The C atoms are orange; H atoms white; and the Fe atoms grayish blue. The atoms far away from the active sites are not shown (that includes the C atom chemisorbed)

second C atom; instead, we use the C atom already on the surface as a reactant. We start both reactions also with a CH_3 chemisorbed on the surface (in addition to one or more C atoms). The methane-forming reactions begins with also a chemisorbed H on the surface.

Let's look at reaction (4) first. Starting with both CH_3 and H adsorbed on threefold sites (Fig. 19), the reaction proceeds by displacement of the H atom towards the CH_3, which does not move much horizontally, but goes up slightly. At the TS (from NEB calculation), the H atom has moved to a different threefold site from its initial position, and the CH_3 radical is slightly lifted up from the surface, by about 0.3 Å. In the final snapshot, the product CH_4 molecule departs from the surface.

For reaction (5) (Fig. 20; we also used the NEB method to locate the TS of the reaction). C–C coupling proceeds in a very different way. Because of the strong binding of a C atom in the fourfold site of the (110) surface (by about 8 eV, as we discussed in the beginning of the work), the C atom

Fig. 18 Three structures with different C permeation levels, preparing for reactivity studies; **a** no C permeation: 1C on the surface; **b** medium permeation: 4C on the surface and 1C permeated to the 2nd layer; **c** high permeation: 4C on the surface, 6C permeated to the 2nd layer, and 1C in the 3rd layer. The C atoms are orange and the Fe atoms grayish blue
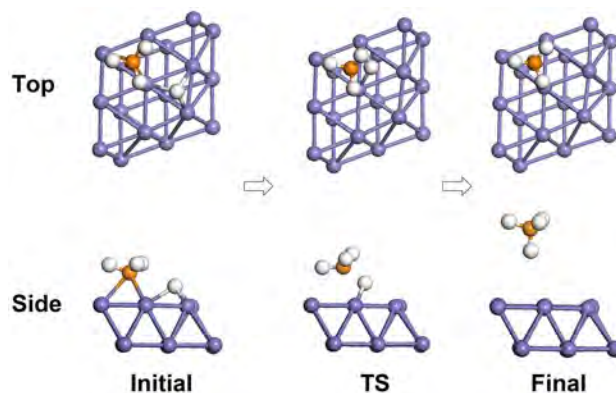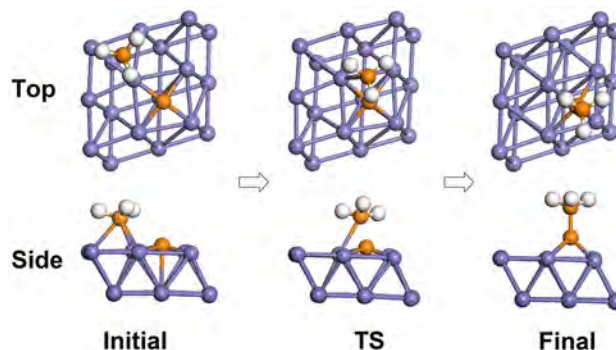

Fig. 20 Top and side views of a C–C coupling reaction on Fe (110) at C coverage of 1C. The C atoms are orange; H atoms white; and the Fe atoms grayish blue

Fig. 21 The energy profiles for CH$_4$ formation and C–CH$_3$ coupling on Fe (110) at different carbon coverages. The reaction and TS energies are in eV. In each case the reaction forming CCH$_3$ on the surface uses one of the carbon atoms on the surface, leaving 0, 4, 10C per cell on or in the slab
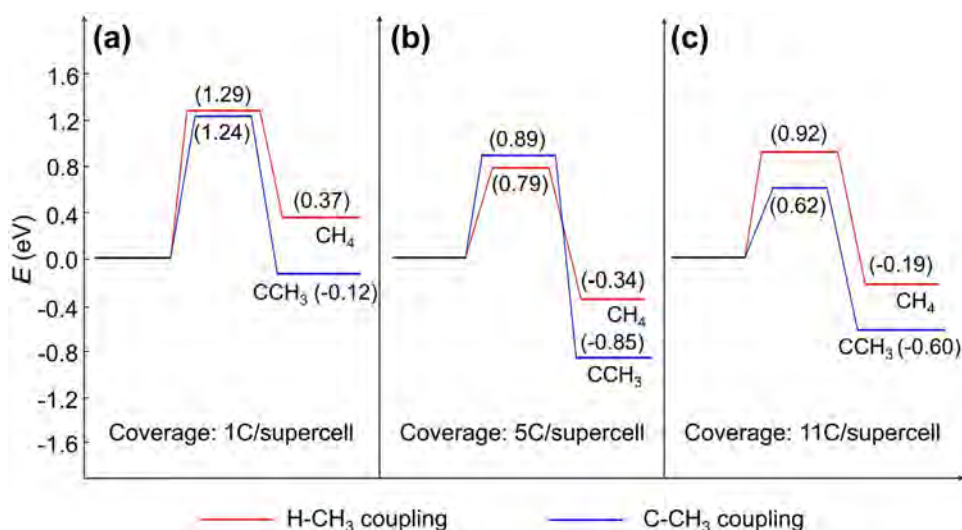
remains fixed at its coordination site during the course of the reaction. It is the CH$_3$ radical that moves towards the top of the C atom, and the reaction ends up with a chemisorbed ethylidyne, C–CH$_3$, with the bottom C atom slightly further away (d = 1.10 Å) from the surface than before (d = 0.35 Å).

What are the barriers for the two reactions? In our calculation, at this C coverage (1C), (Fig. 21a), both the H–CH$_3$ coupling and C–CH$_3$ coupling need to overcome a large yet similar barrier (1.29 and 1.24 eV, respectively). At this coverage we get low activity, and low C–C coupling selectivity on Fe (110).

Now, we add more C atoms sequentially on the surface, up to 5 separate C atoms on the surface in total (5C/supercell, Fig. 21b), with the positions of the C atoms as we discussed in the beginning of the work. In this situation, C permeation occurs: of the 5C atoms, one of them has penetrated the surface. We re-do the TS searches at this new C coverage with the NEB, similar to what we did before at 1C coverage. The barriers (Fig. 21b) required for these two reactions both drop significantly, and CH$_4$ formation emerges as slightly more favored than C–CH$_3$ coupling (0.79 vs. 0.89 eV). The fact that the CH$_4$ formation barrier is lowered at carburized surfaces is in good agreement with the findings by Govender that methane formation on carburized surfaces is faster than on reduced Fe surfaces [8].

As the carbon coverage increases further, to a C coverage of 11C/supercell, much C permeation occurs, with 6C in the 2nd layer and 1C in the 3rd layer (Fig. 21c). Now we calculate that the C–CH$_3$ coupling becomes much more preferable kinetically, requiring significantly less energy (0.62 eV) than CH$_4$ formation (0.92 eV). This computational result is in qualitative agreement with experimental precedent [11, 12]—sufficient carburization is essential to promote the desired C–C coupling, and to suppress undesired CH$_4$ formation. Similar theoretical results are observed on other facets. Our results suggest that carbon permeation not only lowers the reaction barrier significantly, but tunes selectivity such that the preference for the formation of longer hydrocarbon chains is increased. We will return to a possible explanation of this observation in a future study.

11 Conclusions

We investigated, in a variety of ways, the carbon permeation process on models for Fe catalysts, with the aim of elucidating from not one, but several crucial perspectives, how the early stage of C permeation (carbon chemisorption and movement subsurface) affect the Fe-based Fischer–Tropsch process. The aspects studied were thermodynamics, kinetics, the morphological evolution of in-situ catalyst nanoparticles, an electronic property related to catalysis (d-band center), and barriers of key surface reactions.

From an MD simulation (our first approach) of releasing C atoms onto the Fe surfaces, a general picture of the carburization was obtained. Surface carburization can be divided into two stages: an early stage of C permeating into Fe surfaces without much disturbance, and a late stage that causes significant phase transition. With this knowledge, the next five approaches focus only on the first stage of C permeation, and study it as accurately as we can with DFT calculations.

By approaching C atoms sequentially to the surface and undersurface, we found that C binds strongly with the Fe surfaces, but to a different extent. Depending on the surface, at low coverage, the binding strengths are calculated in the order of $(100) > (310) > (110) > (211) > (111)$, and fall in the range of $-7.8-\!-8.5$ eV. The binding strength at all the surfaces studied tends to become weaker as more C atoms are brought into the system, likely because the Fe atoms

are becoming more and more positively charged. On three of the surfaces, (111), (211), and (310), we found that C_2 units form, with C–C bond length in the range of typical C=C double bonds. At certain C coverages, labelled by us as critical branch points, one or more C atoms prefers to go beneath the surface thermodynamically. The coverage where this happens varies with surface.

Calculation of the barriers of permeation at the critical branch point shows that C permeation is kinetically very facile on some surfaces ($E_a = 0.27$ eV for (110)), but difficult on other surfaces ($E_a = 1.64$ eV on (100)). The energy order of the permeation barrier (motion from the surface to below it) is (100) > (111) > (310) > (211) > (110). Examination of the detailed permeation reaction pathways of the two (100) and (110) surfaces, with disparate computed activation energies, suggests that the C permeation barriers are determined by the topology of the surfaces, in other words, the way that Fe atoms are stacked on different surfaces. The reasons for this remain to be determined.

We found that C surface migration and subsurface permeation may be happening at the same time, by comparing the permeation and migration barriers. In particular, the (111) surface prefers migration to permeation for both low and intermediate C coverage. (100) prefers permeation at low C coverage, but migration at intermediate C coverage. All the other surfaces show preferences for permeation for both low and intermediate C coverage.

Using the Wulff construction, we next studied how C permeation might change catalyst nanoparticle geometry. C permeation is computed to change the surface energies of the Fe surfaces in a complicated way: the surface energies of (111), (211), and (110) decrease with C permeation, but those of (100) and (310) first decrease, then increase. Wulff constructions using these surface energies show that in the equilibrium shape of the Fe nanoparticles, the exposed area of the (310) facet first increases with C permeation, then decreases; while the area of (100) first decreases, then increases. The changes, while perceptible, are not dramatic.

C permeation also modulates the electronic structures of pure iron surfaces, as indicated by a change in the energy of the d-band centers and site-dependent charge of the involved surface Fe atoms. For all the surfaces studied, C permeation moves the d-band centers of the surfaces further away from the Fermi level. The effect is substantial: it occurs to the extent that the d-band centers at high C coverage resemble those of various bulk iron carbides (γ-Fe$_4$C, χ-Fe$_5$C$_2$, θ-Fe$_3$C, and ε-Fe$_2$C), which are believed to be among the active catalytic phases in FTS. Analysis of the site-dependent charge of the involved surface Fe atoms (q_{Fe}) shows that Fe surfaces with intermediate C permeation have similar q_{Fe} with χ-Fe$_5$C$_2$ surfaces, indicating likelihood of similar catalytic activity in CO activation of the C permeated Fe surface and an iron carbide phase.

C permeation changes the selectivity of the Fe catalysts in FTS. Using two competing model reactions (C–CH$_3$ and H–CH$_3$ coupling) as example, we found that the barriers of both reactions are generally lowered with increasing C coverage. Moreover, at high C coverage, the desired C–CH$_3$ coupling reaction is significantly preferred to the undesired H–CH$_3$ chain termination. We thus propose that C permeation in iron is beneficial in both activity and selectivity for FTS; this may be one of the key reasons for making iron catalysts the catalyst of choice in FTS.

Our study has limitations. FTS in reality is carried out at high temperatures, allowing the system to go over many barriers which are not reachable in ideal conditions. And there are many complicated physical and chemical processes going on in the FTS reactor. This first work, based on simple models at idealized condition, focuses on the early stage of C permeation and just begins our approach to understanding the carburization process, an in-situ catalyst formation process. In a subsequent paper, we will look at more realistic models for carbon permeation at higher T, try to locate the global minima of C permeated structures, and study the way new surface phases form from the C atoms that have penetrated subsurface.

Overall, we believe that the findings of this study extend our understanding of the C permeation process in the context of FTS, from multiple perspectives. We hope that this knowledge will aid in the discovery of more effective and selective catalysts through surface/interface engineering by modulation of the degree of carburization, and potentially be extended to other catalytic systems in the field of surface carbon-related heterogeneous catalysis.

Compliance with Ethical Standards

Conflict of interest The authors declare no competing financial interest.

References

1. Anderson RB (1984) The Fischer-Tropsch Synthesis. Academic Press, Orlando
2. Dry ME (1982) Hydrocarb Process 61:121
3. Gregor JH (1990) Catal Lett 7:317
4. Fox JM (1993) Catal Rev—Sci Eng 35:169
5. Geerlings JJC, Wilson JH, Kramer GJ, Kuipers HPCE, Hoek A, Huisman HM (1999) Appl Catal A 186:27

6. Li S, Ding W, Meitzner GD, Iglesia E (2002) J Phys Chem B 106:85
7. Gaube J, Klein HF (2008) J Mol Catal A 283:60
8. Govender NS, de Croon MHJM, Schouten JC (2010) Appl Catal A 373:81
9. Pijolat M, Perrichon V, Bussière P (1987) J Catal 107:82
10. Dry ME, Shingles T, Boshoff LJ, Botha CVH (1970) J Catal 17:347
11. Li S, O'Brien RJ, Meitzner GD, Hamdeh H, Davis BH, Iglesia E (2001) Appl Catal A 219:215
12. de Smit E, Beale AM, Nikitenko S, Weckhuysen BM (2009) J Catal 262:244
13. Hofer L, (1956) Catalysis vol 4. Emmett PH (ed). Reinholt, New York
14. Jin YM, Mansker L, Datye AK (1999) Am Chem Soc Div Pet Chem 44:97–99
15. Davis BH (2003) Catal Today 84:83
16. Caceres PG (2006) Mater Charact 56:26
17. de Smit E, Cinquini F, Beale AM, Safonova OV, van Beek W, Sautet P, Weckhuysen BM (2010) J Am Chem Soc 132:14928
18. Panaccione G, Fujii J, Vobornik I, Trimarchi G, Binggeli N, Goldoni A, Larciprete R, Rossi G (2006) Phys Rev B 73:035431
19. Arabczyk W, Narkiewicz U (1997) Vacuum 48:347
20. Arabczyk W, Moszyński D, Narkiewicz U (1999) Vacuum 54:3
21. Arabczyk W, Rausche E, Storbeck F (1991) Surf Sci 247:264
22. Liu X-w, Li Y-w, Wang J-g, Huo C-f (2012) J Fuel Chem Technol 40:202
23. Liu X-W, Huo C-F, Li Y-W, Wang J, Jiao H (2012) Surf Sci 606:733
24. Sorescu DC (2006) Phys Rev B 73:155420
25. Jiang DE, Carter EA (2005) Phys Rev B 71:045402
26. Jiang DE, Carter EA (2003) Phys Rev B 67:214103
27. Begtrup GE, Gannett W, Meyer JC, Yuzvinsky TD, Ertekin E, Grossman JC, Zettl A (2009) Phys Rev B 79:205409
28. Ji J, Duan X, Gong X, Qian G, Zhou X, Chen D, Yuan W (2013) Ind Eng Chem Res 52:17151
29. Archard JF, Rowntree RA (1988) Proc R Soc Lond A 418:405
30. Ding M, Yang Y, Wu B, Li Y, Wang T, Ma L (2014) Energy Procedia 61:2267
31. Cheshkova KT, Bibin VN, Popov BI (1976) React Kinet Catal Lett 4:307
32. Storch G, Golambik N, Anderson R (1954) Synthesis of hydrocarbons from carbon monoxide and hydrogen [Russian translation]. Inostr. Lit., Moscow
33. Karabelchtchikova O. Fundamentals of Mass Transfer in Gas Carburizing Degree of Doctor of Philosophy Worcester Polytechnic Institute 2007
34. Liu X, Zhang C, Li Y, Niemantsverdriet JW, Wagner JB, Hansen TW (2017) ACS Catal 7:4867
35. Zhou X, Mannie GJA, Yin J, Yu X, Weststrate CJ, Wen X, Wu K, Yang Y, Li Y, Niemantsverdriet JW (2018) ACS Catal 8:7326
36. Huo CF, Wu BS, Gao P, Yang Y, Li YW, Jiao H (2011) Angew Chem Int Ed 50:7403
37. Wang T, Wang S, Luo Q, Li Y-W, Wang J, Beller M, Jiao H (2014) J Phys Chem C 118:4181
38. Plimpton S (1995) J Comput Phys 117:1
39. Liyanage LSI, Kim S-G, Houze J, Kim S, Tschopp MA, Baskes MI, Horstemeyer MF (2014) Phys Rev B 89:094102
40. Berendsen HJC, Postma JPM, Gunsteren WFv, DiNola A, Haak JR (1984) J Chem Phys 81:3684
41. Hasnaoui A, Politano O, Salazar JM, Aral G, Kalia RK, Nakano A, Vashishta P (2005) Surf Sci 579:47
42. Jeon B, Van Overmeere Q, van Duin ACT, Ramanathan S (2013) PCCP 15:1821
43. Kresse G, Furthmüller J (1996) Phys Rev B 54:11169
44. Kresse G, Furthmüller J (1996) Comput Mater Sci 6:15
45. Blöchl PE (1994) Phys Rev B 50:17953
46. Kresse G, Joubert D (1999) Phys Rev B 59:1758
47. Perdew JP, Burke K, Ernzerhof M (1996) Phys Rev Lett 77:3865
48. Monkhorst HJ, Pack JD (1976) Phys Rev B 13:5188
49. Methfessel M, Paxton AT (1989) Phys Rev B 40:3616
50. Jónsson H, Mills G, Jacobsen KW (1998) Classical and quantum dynamics in condensed phase simulations. World Scientific, Singapore
51. Zhao S, Liu X-W, Huo C-F, Li Y-W, Wang J, Jiao H (2012) J Catal 294:47
52. Zhao S, Liu X-W, Huo C-F, Li Y-W, Wang J, Jiao H (2015) Catal Struct React 1:44
53. Eyring H (1935) J Chem Phys 3:107
54. Lu J, Behtash S, Faheem M, Heyden A (2013) J Catal 305:56
55. Ackland GJ, Jones AP (2006) Phys Rev B 73:054104
56. Panzner G, Diekmann W (1985) Surf Sci 160:253
57. Wiltner A, Linsmeier C (2004) Phys Status Solidi (a) 201:881
58. Riikonen S, Krasheninnikov AV, Nieminen RM (2010) Phys Rev B 82:125459
59. Shaik S, Rzepa HS, Hoffmann R (2013) Angew Chem Int Ed 52:3020
60. Li J, Croiset E, Ricardez-Sandoval L (2014) PCCP 16:2954
61. Barteau MA, Madix RJ (1982) Surf Sci 115:355
62. Akita M, Hirakawa H, Tanaka M, Moro-oka Y (1995) J Organomet Chem 485:C14
63. Jensen MP, Phillips DA, Sabat M, Shriver DF (1992) Organometallics 11:1859
64. Wijeyesekera SD, Hoffmann R, Wilker CN (1984) Organometallics 3:962
65. LaPointe AM (2003) Inorg Chim Acta 345:359
66. Pauling L (1947) J Am Chem Soc 69:542
67. Cairns JA, Coad JP, Richards EWT, Stenhouse IA (1980) Nature 288:686
68. Nandula A, Trinh QT, Saeys M, Alexandrova AN (2015) Angew Chem Int Ed 54:5312
69. Tang W, Sanville E, Henkelman G (2009) J Phys 21:084204
70. Le Caer G, Dubois JM, Pijolat M, Perrichon V, Bussiere P (1982) J Phys Chem 86:4799
71. Schliehe C, Yuan J, Glatzel S, Siemensmeyer K, Kiefer K, Giordano C (2012) Chem Mater 24:2716
72. Snovski R, Grinblat J, Sougrati M-T, Jumas J-C, Margel S (2014) J Magn Magn Mater 349:35
73. Huo C-F, Wu B-S, Gao P, Yang Y, Li Y-W, Jiao H (2011) Angew Chem Int Ed 50:7403
74. Wang T, Liu X, Wang S, Huo C, Li Y-W, Wang J, Jiao H (2011) J Phys Chem C 115:22360
75. Winterbottom WL (1967) Acta Metall 15:303
76. Wulff G (1901) Z Kristallogr 34:449
77. Biacchi AJ, Schaak RE (2011) ACS Nano 5:8089
78. Kleibert A, Meiwes-Broer KH, Bansmann J (2009) Phys Rev B 79:125423
79. Kleibert A, Rosellen W, Getzlaff M, Bansmann J (2011) Beilstein J Nanotechnol 2:47
80. Hammer B, Norskov JK (1995) Nature 376:238
81. Hammer B, Nørskov JK, (2000) Advances in catalysis, vol 45. In: Song C (ed). Academic Press, Cambridge
82. Chen B, Wang D, Duan X, Liu W, Li Y, Qian G, Yuan W, Holmen A, Zhou X, Chen D (2018) ACS Catal 8:2709
83. Van Der Laan GP, Beenackers AACM (1999) Catal Rev 41:255
84. Schulz H, vein Steen E, Claey M, (1994) Studies in surface science and catalysis, vol 81. In: Curry-Hyde HE, Howe RF (eds). Elsevier, Amsterdam,
85. Huo C-F, Li Y-W, Wang J, Jiao H (2009) J Am Chem Soc 131:14713

86. Pham TH, Qi Y, Yang J, Duan X, Qian G, Zhou X, Chen D, Yuan W (2015) ACS Catal 5:2203
87. Cheng J, Hu P, Ellis P, French S, Kelly G, Lok CM (2010) J Phys Chem C 114:1085

Publisher's Note Springer Nature remains neutral with regard to jurisdictional claims in published maps and institutional affiliations.